Check for updates

Decomposition of organometallic precursor tricarbonyl(trimethylenemethane)ruthenium Ru(C$_4$H$_6$)(CO)$_3^{+/0}$ in the gas phase investigated by thermal desorption spectrometry†

Ken Miyajima, [ID] *[a] Toshiaki Nagata, [ID] [b] Fumitaka Mafuné, [ID] [b] Tomohiro Tsugawa[c] and Ryosuke Harada[c]

Thermal decomposition of an organometallic precursor Ru(C$_4$H$_6$)(CO)$_3^{+/0}$ was observed using gas-phase thermal desorption spectrometry. It was found that the CO ligands were readily released, forming Ru(C$_4$H$_6$)$^+$ at 600 K. Then, Ru(C$_4$H$_4$)$^+$ and Ru(C$_2$H$_2$)$^+$ were produced as a result of sequential H$_2$ and C$_2$H$_2$ release above 800 K. The activation energies of the ligand losses were estimated from the temperature dependences, and were consistent with the available internal energies obtained by DFT calculations. Based on experimental and computational results, Ru(C$_4$H$_4$)$^+$ was identified as a ruthenium complex with unsubstituted cyclobutadiene, [η^4-(C$_4$H$_4$)Ru]$^+$. For the thermal decomposition of neutral Ru(C$_4$H$_6$)(CO)$_3$, the appearance of photoionized Ru(C$_4$H$_6$)(CO) is evidence of CO loss from Ru(C$_4$H$_6$)(CO)$_2$ at 740 K. The decomposition further proceeds above 800 K, forming Ru(C$_4$H$_6$).

1. Introduction

Ruthenium is attracting attention owing to its promising properties such as good thermal, chemical, and mechanical stability, significantly low bulk resistivity ($\sim$7.1 μΩ cm),[1] and catalytic activity. Ruthenium thin films have been well studied in the field of future semiconductor processing, and some reported applications include gate materials as replacements for W, capacitor electrodes for dynamic random access memory (DRAM),[2,3] local interconnects (M0), and narrow metal lines (M1, M2) as diffusion barriers in logic devices.[4,5] Conventionally, ruthenium thin films are deposited using physical vapor deposition methods such as sputtering, evaporation, and chemical vapor deposition (CVD). Ruthenium carbonyl compounds are widely used as organometallic precursors for catalysts and CVD processes.[6–10]

Atomic layer deposition (ALD) is an emerging process that can be used to deposit thin films with extremely uniform and conformal quality.[11–16] A film with a thickness of a few nanometers can be precisely deposited by controlling the number of ALD cycles. In the ALD process, the self-limiting nature of the deposition technique ideally requires moderate thermal stability in the vapor phase and reactivity with the reactant gas on the substrate at a relatively low processing temperature. Gao *et al.* deposited Ru thin films using η^4-2,3-dimethylbutadiene ruthenium tricarbonyl [Ru(DMBD)(CO)$_3$] with H$_2$O as the reaction gas at a deposition rate of 0.1 nm per cycle at a steady-state deposition temperature of 160–210 °C.[13] They proposed that the ligand dimethylbutadiene is desorbed when the molecule is adsorbed on the surface, while CO forms CO$_2$ and H$_2$ in the water–gas shift (WGS) reaction catalyzed by the Ru metal center. Schneider *et al.* investigated the growth mechanism of Ru thin films using *in situ* quartz-crystal microbalance and quadrupole mass spectrometry for the same Ru(DMBD)(CO)$_3$.[16] They found no evidence of WGS reaction. They proposed that the dominant Ru deposition mechanism is *via* the thermal desorption of labile CO ligands, regenerating active sites for further Ru precursor adsorption. Although the detailed reaction mechanism is not yet clear, the difference in the ease of desorption between the two ligands can be used to select the deposition temperature and control the properties of the Ru thin film. Information on the bond dissociation and activation energies of individual precursors in the intrinsic thermal decomposition mechanism is useful for determining the deposition process conditions.

[a] KOMEX, School of Arts and Sciences, The University of Tokyo, Komaba, Meguro, Tokyo 153-8902, Japan. E-mail: miyajima@cluster.c.u-tokyo.ac.jp

[b] Department of Basic Science, School of Arts and Sciences, The University of Tokyo, Komaba, Meguro, Tokyo 153-8902, Japan

[c] Chemical Materials Development Department, Global Marketing/R&D Supervisory Department, TANAKA PRECIOUS METAL TECHNOLOGIES Co., Ltd., 22, Wadai, Tsukuba, Ibaraki 300-4247, Japan

† Electronic supplementary information (ESI) available: Schematic of the cluster source, mass spectra, structural changes and differences in the formation energies of CO and H$_2$ desorption processes, estimated activation energies for the thermal decomposition reactions, and atomic coordinates of DFT-calculated structures. See DOI: https://doi.org/10.1039/d5cp00200a

9244 | *Phys. Chem. Chem. Phys.*, 2025, **27**, 9244–9251

This journal is © the Owner Societies 2025

In our previous study, the thermal decomposition of tri-ruthenium dodecacarbonyl $Ru_3(CO)_{12}$ in the gas phase was investigated using photoionization mass spectrometry and thermal desorption spectrometry (TDS).[17] It was found that CO ligand molecules were sequentially released in the temperature range 400–900 K, forming Ru_3. Among the intermediate cluster compositions, $Ru_3(CO)_7$ was the most thermally durable cluster, whereas $Ru_3(CO)_3$, $Ru_3(CO)_5$, and $Ru_3(CO)_{10}$ were less durable and decomposed within a narrow temperature range.

Kotsugi *et al.* reported the ALD of a Ru metal–organic precursor, tricarbonyl(trimethylenemethane)ruthenium, Ru(tmm)-$(CO)_3$ (tmm = trimethylenemethane, C_4H_6), with O_2 as a reactant.[18] They found that the simple and small molecular structure of the precursor weakened the intermolecular forces in the liquid phase, resulting in high vapor pressure at room temperature. Additionally, the relatively small ligands of the precursor facilitate efficient ALD, and typical self-limiting growth is observed along with significantly high growth per cycle (GPC) (~ 1.7 Å) at a moderate temperature (493 K). The Ru precursor permits enhanced nucleation and GPC at relatively low deposition temperatures to construct high-quality Ru films with significantly low resistivity using simple, plasma-free techniques and is suitable for the fabrication of emerging Ru films to replace Cu-based interconnects. Unlike homoleptic precursors such as $Ru_3(CO)_{12}$, the deposition can be more precisely controlled by temperature and coreactant conditions when using two different ligands.

$Ru(C_4H_6)(CO)_3$, $[[\eta^4\text{-}((CH_2)_3C)]Ru(CO)_3]$, is one of the 18 electron systems:[19] The Ru atom donates two electrons to tmm,[20] forming Ru^{2+} and $C_4H_6^{2-}$, and it comprises six d-electrons from Ru^{2+}, six π-electrons from $C_4H_6^{2-}$, and six electrons from three CO ligands. Therefore, they are stable organometallic compounds that can be handled in the air. Additionally, this compound has a heteroleptic coordination environment, in contrast to the simple Ru carbonyl cluster $Ru_3(CO)_{12}$, which exhibits homoleptic coordination of the CO ligands. As a mentioned above, typical self-limiting growth and an ALD temperature window of 493–513 K are observed in the deposition system using $Ru(C_4H_6)(CO)_3$ with O_2, but the ALD system using $Ru_3(CO)_{12}$ as a precursor has not been reported so far, probably for the less thermal stability. Therefore, information on the thermal properties of the precursor is attractive for understanding the differences in the effects of coordinated ligands between organometallic and metal carbonyl compounds such as $Ru_3(CO)_{12}$.

To elucidate the intrinsic thermal decomposition mechanism, it is important to investigate the precursor compound in the gas phase, which is free from complicated interactions with substrate materials and other chemical species.[21] In this study, the thermal decomposition of $Ru(C_4H_6)(CO)_3$, $[[\eta^4\text{-}((CH_2)_3C)]\text{-}Ru(CO)_3]$, was investigated.[22,23] The products of thermal decomposition were identified using temperature-variable mass spectrometry by observing the native cationic species formed by laser plasma or photoionized species using an F_2 laser. The activation energies of the thermal decomposition process were calculated and discussed.

2. Methodologies

Thermal decomposition of $Ru(C_4H_6)(CO)_3^{+/0}$ in the gas phase was investigated using TDS and mass spectrometry. The details of the experimental setup have been previously reported.[17,24] Therefore, the cluster generation and mass spectrometry sections of the experimental setup are outlined here. A liquid of $Ru(C_4H_6)(CO)_3$ (TANAKA PRECIOUS METAL TECHNOLOGIES Co., Ltd.) was loaded into a short 1/4-inch Teflon tube connected *via* a 1/4-inch stainless steel T-joint to the helium carrier gas line upstream of the general valve, as shown in Fig. S1 (ESI†). Sufficient vapor pressure was obtained without increasing the temperature of the vapor source.[18] $Ru(C_4H_6)(CO)_3$ vapor was mixed with 0.17% O_2 ($> 99.9\%$) seeded He gas or pure He gas ($> 99.99995\%$; 0.62 MPa) and introduced into the vacuum chamber *via* a pulsed valve. It is common to mix oxidizing or non-oxidizing reaction gases, such as oxygen, water, and hydrazine, as coreactants in industrial applications such as ALD. In this study, helium gas mixed with oxygen was used as a gas to transport precursor vapor, but no changes due to oxidation of the precursor or pyrolysis products were observed. However, it was observed that molecular oxygen attachments were formed and that they desorbed O_2 upon heating.

When we carried out mass spectrometry without photoionization by an F_2 laser, $Ru(C_4H_6)(CO)_3$ was ionized by laser plasma, which was formed by irradiating a Ru metal rod (99.95%, 5 mm dia.) with a focused pulse laser (second harmonic of a Nd:YAG laser; 532 nm, 10 Hz, ~ 6 mJ per pulse) downstream of the pulsed nozzle. The carrier gas pulse passed through an extension tube (copper tube, 10 mm outer diameter, 4 mm inner diameter, 116 mm length) in which the temperature was controlled in the range of 300–1022 K. The residence time of the species in the carrier gas pulse in the tube was estimated to be approximately 100 μs, and the number density of the helium atoms exceeded 10^{18} cm^{-3}. Hence, the molecules underwent more than 10 000 collisions with helium, ensuring that thermal equilibrium was achieved in the tube.

For mass analysis, the reaction products in the carrier gas were expanded into vacuum at the end of the extension tube. After passing through a skimmer, the ions gained kinetic energy of 3.5 keV in the acceleration region. To measure the neutral species, they were photoionized by an F_2 laser (MPB PSX-100, ~ 0.4 mJ cm^{-2}). The ions traveled in a 1 m field-free region and were reflected by a dual-stage reflectron. Subsequently, they were detected using a Hamamatsu double-microchannel plate detector. The averaged time-of-flight (TOF) spectra (averaged over 200 sweeps) were sent to a computer for analysis. The mass resolution was sufficiently high ($m/\Delta m \approx 600$ at $m/z = 240$) to distinguish isotopic peaks in the mass spectra. The attribution of the mass spectra observed at 303 and 1022 K by the peak distribution of the isotope distribution for each species is shown in Fig. S2 of ESI.† Thermal desorption spectra were recorded under the same conditions while heating the extension tube at a linear heating rate of 8.7 K min^{-1}.

The stable geometries of $Ru(C_4H_6)(CO)_k^{+/0}$ ($k = 1$–3), $Ru(C_4H_6)^{+/0}$, and $Ru(C_4H_4)^{+/0}$ were obtained by quantum chemical calculations using Gaussian 16.[25] ωB97X-D and Def2-TZVPP basis sets were

This journal is © the Owner Societies 2025

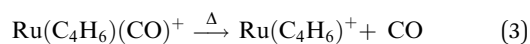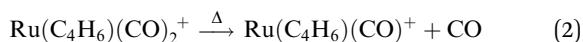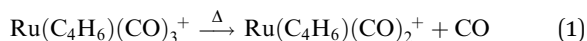*Phys. Chem. Chem. Phys.*, 2025, **27**, 9244–9251 | **9245**

used for the calculations. Here, the inner 28 electrons of Ru atoms are treated as a frozen core by an effective core potential that accounts for relativistic effects. Natural bond orbital (NBO) analyses were also performed to calculate atomic charges and spin densities.[26,27] The optimized isomers were examined using vibrational frequency calculations to ensure that the optimized structures reflected the true potential minimum. All calculated energies described below include the zero-point vibrational energy correction. The internal available energy was calculated using thermal analysis based on the calculated vibrational frequencies. Binding energy was calculated as the difference like $E(Ru(C_4H_6)(CO)_{k-1}^+) + E(CO) - E(Ru(C_4H_6)(CO)_k^+)$. The formation energy in this study refers to the sum of the electronic and zero-point vibrational energies.

3. Results and discussion

3.1. Thermal decomposition of $Ru(C_4H_6)(CO)_3^+$ at different temperatures

To observe the thermal decomposition of $Ru(C_4H_6)(CO)_3^+$, the ion was heated in He carrier gas inside the extension tube in the presence of O_2. The mass spectra obtained at different temperatures are shown in Fig. 1(a). At 303 K, mass peaks corresponding to $Ru(C_4H_6)(CO)_3^+$ are predominantly observed. The appearance of these peaks proves that the intact $Ru(C_4H_6)(CO)_3$ molecule, introduced into the vacuum, was ionized by the laser plasma without any significant fragmentation. At higher temperatures, mass peaks of $Ru(C_4H_6)^+$ were observed at 700 K, and those of $Ru(C_4H_4)^+$ and $Ru(C_2H_2)^+$ were observed at 1000 and 1022 K. It is evident that the thermal decomposition of the tmm ligand occurred at higher temperatures.

To closely examine the variation in the product species with temperature, an intensity map and TDS plot were obtained, as shown in Fig. 1(b) and Fig. 2. Evidently, $Ru(C_4H_6)(CO)_3^+$ remained intact within the temperature range of 300–500 K. Decomposition by CO loss proceeded sequentially in the temperature range of T = 500–700 K.

$$Ru(C_4H_6)(CO)_3^+ \xrightarrow{\Delta} Ru(C_4H_6)(CO)_2^+ + CO \qquad (1)$$

$$Ru(C_4H_6)(CO)_2^+ \xrightarrow{\Delta} Ru(C_4H_6)(CO)^+ + CO \qquad (2)$$

$$Ru(C_4H_6)(CO)^+ \xrightarrow{\Delta} Ru(C_4H_6)^+ + CO \qquad (3)$$

Note that the O_2 adduct ions $Ru(C_4H_6)(CO)_2(O_2)^+$ and $Ru(C_4H_6)(CO)(O_2)^+$ were also observed in the intensity map, which is not the main scope of the present study. $Ru(C_4H_6)(CO)_3(O_2)^+$ was not observed, suggesting that $Ru(C_4H_6)(CO)_3^+$ has no empty sites on the Ru atom where oxygen molecules can coordinate and that CO is more strongly bound to Ru than O_2.

To verify the effect of oxygen addition, a parallel experiment was conducted using helium carrier gas without oxygen. We begin with the differences observed in the mass spectra of the positive ions without heating. As shown in Fig. S3 of the ESI,† mass peaks of dimer, $[Ru_3(C_4H_6)(CO)_3]_2^+$, and peaks resulting
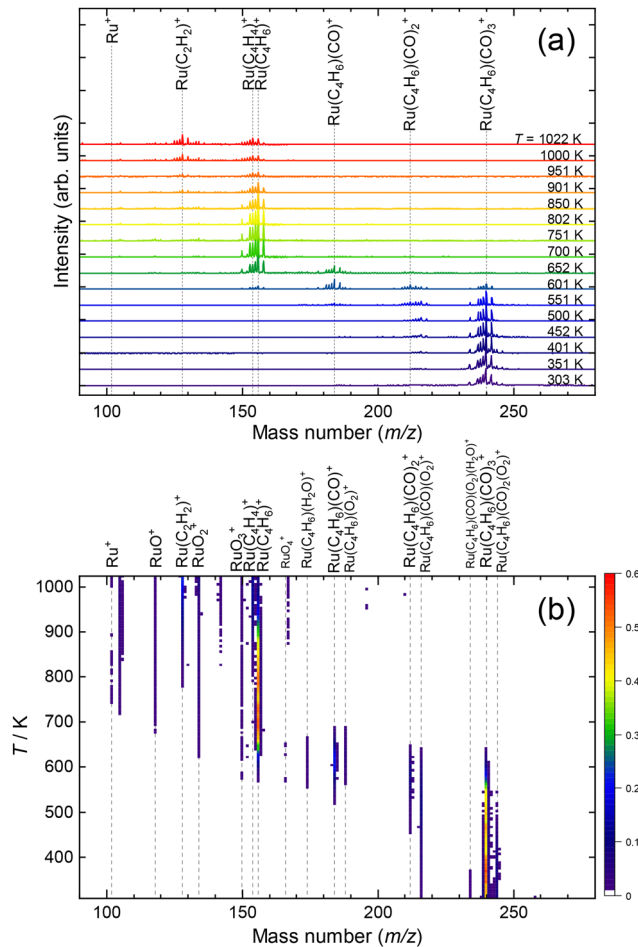

Fig. 1 (a) Mass spectra of the species produced by thermal decomposition of $Ru(C_4H_6)(CO)_3^+$ in 0.17% O_2 seeded helium carrier gas at different temperatures. (b) Two-dimensional plot of mass spectra after deconvolution using the isotopic pattern of the Ru atom. The total ion intensity was normalized at each temperature.
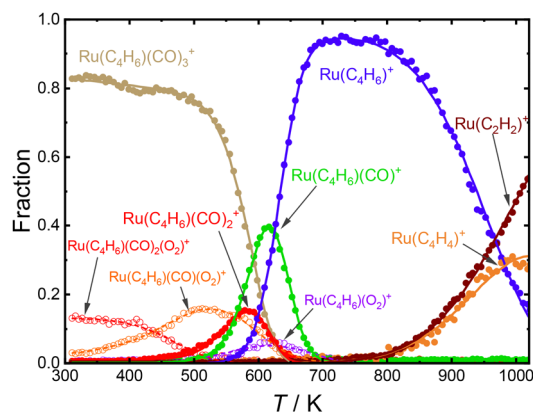

Fig. 2 Fractions of species generated by thermal decomposition of $Ru(C_4H_6)(CO)_3^+$ in 0.17% O_2 seeded helium carrier gas as a function of the extension tube temperature. The curves show the results of curve fitting assuming sequential CO, H_2, and C_2H_2 releases. O_2 adducts are indicated by the open circles and dashed lines.
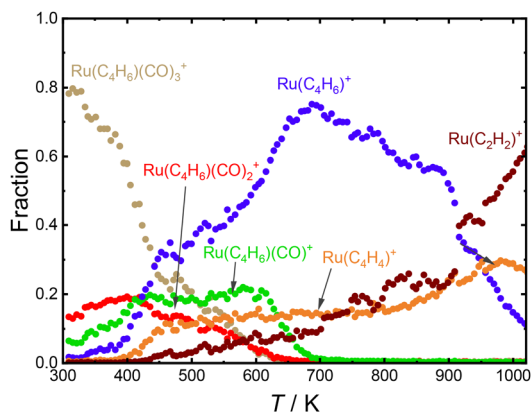
Fig. 3 Fractions of species generated by thermal decomposition of $Ru(C_4H_6)(CO)_3{}^+$ in pure helium carrier gas as a function of the extension tube temperature. To reduce complexity, this analysis excluded proton-attached and water-attached ions such as $Ru(C_4H_6)(CO)_3H^+$ or $Ru(C_4H_6)(H_2O)^+$.

from gradual CO desorption were observed on the heavy side of the mass spectrum, although weak. The amount of compositions resulting from CO desorption was higher in the absence of oxygen than in the presence of oxygen. The intensities of these minor peaks were sufficiently weak compared with those of the $Ru_3(C_4H_6)(CO)_3{}^+$ monomer, and their decomposition contributions were not included in the analysis.
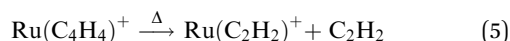
The TDS plot for the case without oxygen in the He carrier gas is shown in Fig. 3. The TDS curves showed a more complex shape over a wider temperature range than those in the presence of oxygen and did not clearly separate each step of the desorption reaction. The curves shown in Fig. 3 without oxygen showed large fluctuations, whereas those in Fig. 2 with oxygen exhibited small fluctuations.

Comparing the cases with and without oxygen, a commonality is found in the upper temperature limits: $Ru(C_4H_6)(CO)_{2,3}{}^+$ disappeared at 650 K, whereas $Ru(C_4H_6)(CO)^+$ disappeared at 700 K in both cases. The ratios of $Ru(C_4H_6)^+$, $Ru(C_4H_4)^+$, and $Ru(C_2H_2)^+$ at 950–1022 K were almost identical. Although the upper limits of the observed temperatures were the same, in the absence of oxygen, clusters with CO already coexisted even at room temperature as shown in Fig. S3 (ESI†), and the percentage of such clusters gradually increased up to 700 K. The changes observed at 500–700 K in the presence of oxygen started at room temperature and slowly progressed over a wide temperature range of 300–700 K in the absence of oxygen. Possible explanations for the differences observed with and without oxygen are as follows. (1) Oxygen quenched the excited helium atoms produced by the laser plasma, reducing the decomposition of the precursor and increasing the amount of ionized intact Ru-containing species because of soft ionization. (2) In the presence of oxygen, the excess energy gained by collisions with plasma-derived excited species in the ionization process was initially removed by the release of oxygen molecules, which were more weakly attached than CO and C_4H_6, and consequently the desorption of CO was suppressed in the low temperature range.

It is estimated that the distribution of precursor-related compositions observed in the absence of oxygen, including

water-attached and protonated ions, is sensitive to laser plasma conditions and possibly affects the distribution of the reaction products of $Ru(tmm)(CO)_3$ molecules. This may explain why the fluctuations in the data in Fig. 3 were larger than those with oxygen shown in Fig. 2.

Above 700 K, all the three CO ligands were completely removed, and the $Ru(C_4H_6)^+$ was exclusively produced. With a further increase in temperature, $Ru(C_4H_6)^+$ decreased, and $Ru(C_4H_4)^+$ and $Ru(C_2H_2)^+$ increased gradually above 800 K. The concomitant intensity changes suggest that $Ru(C_4H_4)^+$ was generated by the dehydrogenation of $Ru(C_4H_6)^+$. The reaction proceeded further, releasing acetylene from $Ru(C_4H_4)^+$ to form $Ru(C_2H_2)^+$.

$$Ru(C_4H_6)^+ \xrightarrow{\Delta} Ru(C_4H_4)^+ + H_2 \quad (4)$$

$$Ru(C_4H_4)^+ \xrightarrow{\Delta} Ru(C_2H_2)^+ + C_2H_2 \quad (5)$$

In the presence of oxygen, $Ru(C_4H_4)^+$ and $Ru(C_2H_2)^+$ were not formed until 800 K. In the absence of oxygen, $Ru(C_4H_4)^+$ gradually increases from 400 K, which is also on the lower side. These results suggest that in the presence of oxygen, the oxygen molecules inhibit CO desorption, and the tmm ligand changes by some mechanism.

3.2. Geometrical structures

Fig. 4 shows the geometrical structures of $Ru(C_4H_6)(CO)_{0-3}{}^+$ and $Ru(C_4H_4)(CO)_{0-3}(H_2)^+$ calculated using DFT calculations. The atomic coordinates of the DFT-calculated structures and the natural charges and spins of the atoms obtained by NBO analysis are shown in Table S1 (ESI†). The most stable structures of both the cations and neutrals of $Ru(C_4H_6)(CO)_{0-3}{}^{+/0}$ are shown in Fig. S4 of the ESI.† There was little difference in the appearance of the most stable structures of positive ions and neutrals. The shape of the neutral $Ru(C_4H_6)(CO)_3$ is similar to that of a piano stool, like $Fe(C_4H_4)(CO)_3$, except that the ligand is square or umbrella-shaped, as shown in Fig. 5.

The stable spin state was found to be a doublet for all the ions. Thus, the delegated ions, $Ru(C_4H_6)(CO)_{0-2}{}^+$, retained the original geometries of the piano stool. The obtained

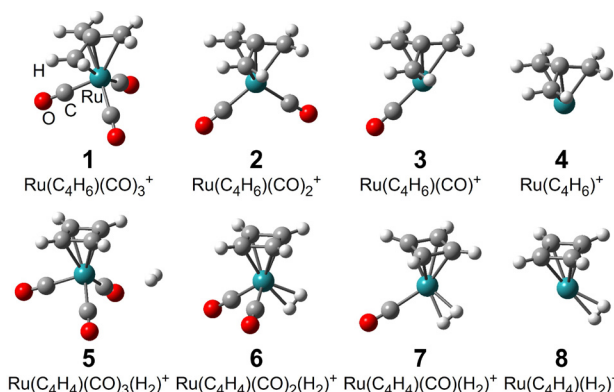Fig. 4 The most stable structures of $Ru(C_4H_6)(CO)_{0-3}{}^+$, **1–4,** and $Ru(C_4H_4)(CO)_{0-3}(H_2)^+$, **5–8**.

This journal is © the Owner Societies 2025

Phys. Chem. Chem. Phys., 2025, **27**, 9244–9251 | **9247**

Fig. 5 Geometrical structures of $Fe(C_4H_4)(CO)_3$[28] and $Ru(C_4H_6)(CO)_3$,[23,29] and a photograph of a vintage piano stool owned by the author.

geometrical structures of $(CH_2)_3CRu(CO)_{1-3}$ resemble the optimized structure of the analogs of iron, umbrella-shaped trimethylene-methane complexes, $(CH_2)_3CFe(CO)_{1-3}$.[30] For $Ru(C_4H_6)(CO)_3^+$, the tmm ligand leans slightly, and one of the outer C atoms binds farther than the other two C atoms. According to the NBO analysis, this C atom carries a high spin density (+0.60e), suggesting that the p-electron was removed upon ionization. Namely, tmm is regarded as singly charged, tmm^{1-}, in $Ru(C_4H_6)(CO)_3^+$, although tmm is doubly charged in neutral $Ru(C_4H_6)(CO)_3$. In contrast, $Ru(C_4H_6)^+$ shows nearly C_{3v} symmetry, in which all three peripheral C atoms bind equidistantly to the Ru atom. Indeed, NBO analysis shows that all the peripheral C atoms carry similar low spin densities (ca. −0.08e), suggesting that tmm is doubly charged in $Ru(C_4H_6)^+$. Instead, the Ru atom has a high spin density (+1.19e), which can be explained by the fact that the Ru atom is ionized to Ru^{3+} with five d-electrons.

3.3. Activation energy of the CO loss

Since each TDS curve in Fig. 2 represents the ion intensity as a function of temperature, the activation energy of ligand release, E_a, can be estimated using the Arrhenius equation.[24] Table 1 and Fig. S5 (ESI†) summarize the activation energies of each step. Activation energies were estimated from repeated measurements. The first two steps showed good reproducibility, whereas the third step exhibited a larger variation, likely due to the narrower temperature range over which this process occurred. The activation energy of reaction (1) is higher than those of reactions (2) and (3), which can be interpreted as destabilization with a decrease in the CO ligands.

We also obtained the available internal energies of the ions at the ligand loss temperatures, which correspond to the total vibrational energies above the zero-point energies (Table 1) in the DFT calculations. Note that the vibrational degree of freedom decreased with the loss of the ligand, and the available energy also decreased, even at the same temperature.

Table 1 Activation energy of each step estimated from the TDS curves, available energy of the ions at 600 K, and binding energy of CO calculated for stable geometries of $Ru(C_4H_6)(CO)_k^+$ ($k = 0-3$) in eV

Reaction	Activation energy (exptl.)	Available energy	Binding energy
$k = 3 \to 2$	0.95 ± 0.01	0.90	1.50
$k = 2 \to 1$	0.63 ± 0.01	0.67	1.32
$k = 1 \to 0$	0.66 ± 0.06	0.52	1.53

The available energies of the ions at the ligand loss temperatures are almost the same as the activation energies, which indicates that the ions overcome the activation barrier with their internal energies, consistent with the basic idea of the RRK theory.[31,32] The concept of available energy represents the total vibrational energy accessible at a given temperature, calculated as the sum of vibrational mode populations above the zero-point energy. While the activation energy represents the energetic barrier for CO dissociation, the available energy defines the portion of internal energy that can contribute to overcoming this barrier.

The agreement between these two values suggests that CO dissociation proceeds through an energy redistribution mechanism, where internal vibrational energy plays a key role in surpassing the activation barrier. This trend suggests that the activation energy is effectively governed by the internal energy available within the cluster, rather than solely by the intrinsic CO binding strength. As the number of ligands decreases, the reduction in vibrational degrees of freedom limits the available energy for overcoming the barrier, leading to the observed stepwise decrease in activation energy.

However, a puzzling issue remains: The activation energy for the CO loss should be almost the same as the binding energy of CO, as the release of CO does not require significant structural changes. This apparent discrepancy may be explained by considering that the experimental activation energies are lower than the computed binding energies because, at high temperatures, CO dissociation is facilitated not only by the energy difference between the initial and final states of CO release, but also by the redistribution of internal vibrational energy within the molecule.

Nevertheless, the activation energies of CO desorption from $Ru(C_4H_6)(CO)_k^+$ for the experimental TDS process were estimated to be 0.95 eV ($k = 3$), 0.63 eV ($k = 2$), and 0.66 eV ($k = 1$), which are consistent with the typical binding energy of CO to the transition metal atoms, such as $Fe(CO)_x^+$ and $Cr(CO)_x^+$.[33,34] The experimentally observed activation energies were much lower than the binding energies. This difference cannot be explained by the simple release of CO. We simulated the possibility that the precursor ion takes a different form $Ru(C_4H_4)(CO)_3(H_2)^+$, **5**, with cyclobutadiene and H_2 ligands. The formation energy from the most stable structure for the isomer is less stable than **1**, +1.11 eV. The Ru–CO binding energies in **5**, **6**, and **7** were 0.91, 1.44, and 1.38 eV, respectively. Thus, the energy of the first CO loss decreased slightly, but the energies required for the subsequent steps were almost the same as those for **1–4**. To clarify the details of the observed pyrolysis process, it is necessary to discuss the energy differences and reaction rates between several coexisting intermediates.[35] If the back-and-forth between isomers is sufficiently fast to be regarded as equilibrium, the energy weighted by the equilibrium ratio is the effective energy.[36]

3.4. Structures for $Ru(C_4H_4)^+$

Wasendrup et al. investigated reactivity of M^+ (M = Ru and Rh) with butadiene and acetylene (ethyne), finding that

9248 | Phys. Chem. Chem. Phys., 2025, **27**, 9244–9251
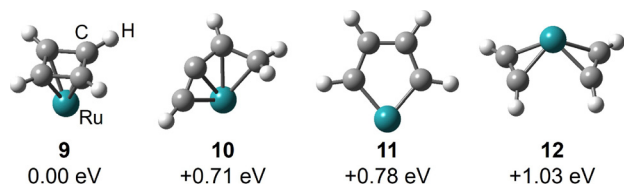
This journal is © the Owner Societies 2025

Fig. 6 Stable structures of RuC$_4$H$_4$$^+$, **9–12**, determined by DFT calculations. The formation energies from the most stable structure, **9**, are also shown.

dehydrogenation of butadiene by M$^+$ generates MC$_4$H$_4$$^+$:[37] The key intermediate reacted with ethyne to yield benzene C$_6$H$_6$ and bare M$^+$. Structural investigations of MC$_4$H$_4$$^+$ by collision-induced dissociation and ion–molecule reactions suggested that metallacyclopentadiene, or a structure with a C–C–C–C–Ru five-membered ring, for RuC$_4$H$_4$$^+$ and a rhodium–cyclobutadiene complex were the most probable structures. In the present study, we observed an ion with the same stoichiometry generated *via* the dehydrogenation of Ru(C$_4$H$_6$)$^+$. Although the structure of RuC$_4$H$_4$$^+$ generated by thermal decomposition does not need to be the same as that of the key intermediate for the catalytic formation of benzene, the formation of a species with the same stoichiometry is interesting. Now, a question arises regarding the geometrical structure of RuC$_4$H$_4$$^+$.
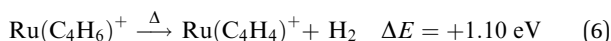
$$Ru(C_4H_6)^+ \xrightarrow{\Delta} Ru(C_4H_4)^+ + H_2 \quad \Delta E = +1.10 \text{ eV} \quad (6)$$

Fig. 6 shows the stable structures of RuC$_4$H$_4$$^+$ obtained by DFT calculations. The most stable structure is ruthenium–cyclobutadiene complex, **9**. The geometrical structure and spin density show that all four C atoms are equivalent, suggesting that C$_4$H$_4$ is a dianion. Hence, this complex was considered to be composed of Ru^{3+} and C$_4$H$_4$$^{2-}$. The significant stability of this complex is considered to originate from the aromaticity of C$_4$H$_4$$^{2-}$, which satisfies the Hückel rule.[19] For neutral RuC$_4$H$_4$, the ruthenium–cyclobutadiene complex was not the most stable among the possible isomers because the charge state of the Ru atom was +2, which may not be the stable charge state for Ru (Fig. 7). Based on the formation energy, the dehydrogenation reaction is calculated to be endothermic by 1.10 eV.

The second most stable structure is metallacyclopentadiene (*cis*-1,3-butadiene-1,4-diyl coordinated Ru), **10**, the third one is 1-butene-3-yne coordinated Ru complex, **11**, and the fourth one is bis-(ethyne) complex, **12**. However, their formation energies are quite high compared to **9**. Furthermore, the activation energy of dehydrogenation is higher, considering that dehydrogenation requires significant structural changes. In
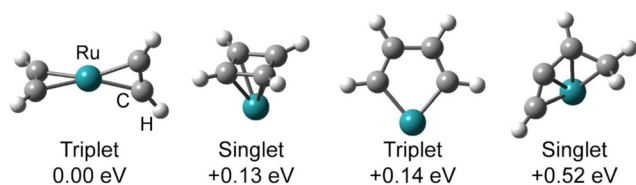

Fig. 8 Two-dimensional plot of the mass spectrum of the decomposition products of neutral Ru(C$_4$H$_6$)(CO)$_3$ seeded in helium carrier gas as a function of the extension tube temperature. The products were photo-ionized by irradiation with an F$_2$ excimer laser at 157 nm (7.87 eV). This spectrum was simplified by deconvolution of the isotopic pattern of the Ru atom. To account for the fact that the sum of intensities is not conserved because of the presence of species with high ionization energy that cannot be photoionized by a single photon, the observed ion intensities are directly color-coded rather than relative intensities at each temperature.

contrast, the experimentally observed activation energy of dehydrogenation was 1.12 eV. This value was comparable to the available internal energy of RuC$_4$H$_6$$^+$ at 900 K (0.76 eV). Hence, the formation of complexes **10–12** is not plausible. We concluded that complex **9** was the only accessible complex.

3.5. Thermal decomposition of *neutral* Ru(C$_4$H$_6$)(CO)$_3$

The thermal decomposition mechanism of neutral compounds has attracted considerable attention for application as precursors for CVD/ALD.[9,38] The TDS plot of neutral Ru(C$_4$H$_6$)(CO)$_3$, shown in Fig. 8, was interpreted based on the results of the cationic compound and DFT calculations. Note that no oxygen was added and only He was used as the carrier gas in this neutral species measurement. Unfortunately, Ru(C$_4$H$_6$)(CO)$_3$ and Ru(C$_4$H$_6$)(CO)$_2$ were not observed in this study. In the present experiment, the species produced by thermal decomposition at different temperatures were irradiated with an F$_2$ excimer laser at 157 nm (7.87 eV); hence, only the species with ionization energies lower than 7.87 eV were photoionized and mass analyzed. The ionization energy of a Ru atom is known (7.36 eV);

Fig. 7 Stable structures of neutral RuC$_4$H$_4$ obtained by DFT calculations. The formation energy with respect to the most stable structure is also shown.
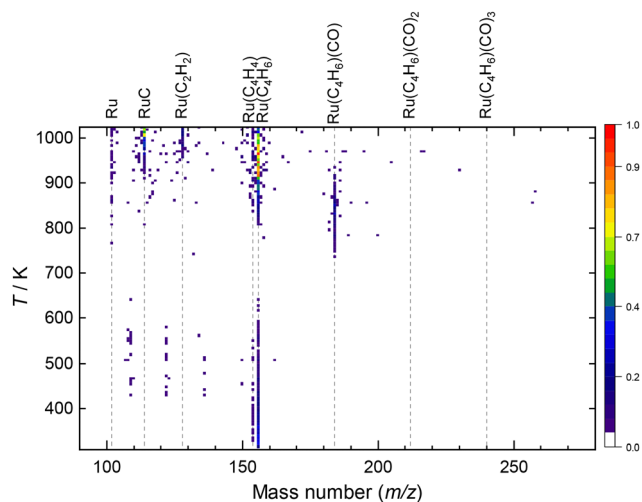
Table 2 Ionization energy of the species that can be produced by thermal decomposition obtained by DFT calculations in eV

Species	Ionization energy
Ru(C$_4$H$_6$)(CO)$_3$	9.11
Ru(C$_4$H$_6$)(CO)$_2$	8.55
Ru(C$_4$H$_6$)(CO)	7.68
Ru(C$_4$H$_6$)	6.87
Ru(C$_4$H$_4$)	6.15
Ru(C$_2$H$_2$)	7.06
RuC	7.42

This journal is © the Owner Societies 2025

*Phys. Chem. Chem. Phys.*, 2025, **27**, 9244–9251 | **9249**

hence, the Ru atom can be ionized. For other species that were possibly produced by thermal decomposition, the vertical ionization energies were obtained by DFT calculations (see Table 2).

The ionization energies of the intact $Ru(C_4H_6)(CO)_3$ and $Ru(C_4H_6)(CO)_2$ were so high that these species could not be photoionized. As we confirmed that $Ru(C_4H_6)(CO)_3$ was introduced inside vacuum in an intact form, the missing signal at 300–500 K suggests $Ru(C_4H_6)(CO)_3$ and/or $Ru(C_4H_6)(CO)_2$. Appearance of $Ru(C_4H_6)(CO)^+$ is the clear evidence of the CO loss occurring at 740 K as

$$Ru(C_4H_6)(CO)_2 \xrightarrow{\Delta} Ru(C_4H_6)(CO) + CO. \quad (7)$$
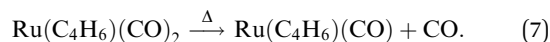
The decomposition proceeded further above 800 K, forming $Ru(C_4H_6)$.

$$Ru(C_4H_6)(CO) \xrightarrow{\Delta} Ru(C_4H_6) + CO \quad (8)$$
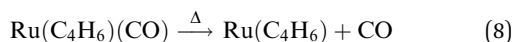
The dehydrogenation of $Ru(C_4H_6)$ was observed to form $Ru(C_4H_4)$; however, its abundance was lower than that of cationic ions. This is consistent with the fact that neutral RuC_4H_4 is not very stable, as the charge state of the Ru atom is +2, which may not be the stable charge state for Ru. In the neutral case, RuC was abundantly formed at higher temperatures. Although the formation mechanism is unknown, it is highly likely that RuC was generated by the thermal decomposition of the ligand.

$Ru(C_4H_6)$ and $Ru(C_4H_4)$ were observed even at 300 K, suggesting that $Ru(C_4H_6)$ and $Ru(C_4H_4)$ may co-exist in the original sample. However, we consider that the amounts of $Ru(C_4H_6)$ and $Ru(C_4H_4)$ were sufficiently low because the intensities of $Ru(C_4H_6)^+$ and $Ru(C_4H_4)^+$ were lower than the noise level in the cationic mode. The ion intensities in the neutral mode are highlighted because of their low ionization energy and high ion detection efficiency at lower temperatures.

Conclusions

Thermal decomposition of cationic $Ru(C_4H_6)(CO)_3^+$ and neutral $Ru(C_4H_6)(CO)_3$ was observed using gas-phase thermal desorption spectrometry. It was found that CO ligands were readily released, forming $Ru(C_4H_6)^+$ at 600 K. Subsequently, $Ru(C_4H_4)^+$ and $Ru(C_2H_2)^+$ were produced as a result of H_2 and C_2H_2 release above 800 K. Based on the experimental and computational results, $Ru(C_4H_4)^+$ was identified as a ruthenium complex with unsubstituted cyclobutadiene, which is composed of Ru^{3+} and $C_4H_4^{2-}$. The high stability of this complex originates from the aromaticity of $C_4H_4^{2-}$, which satisfies the Hückel rule. The activation energy of ligand loss was estimated from the temperature dependence and was found to be consistent with the available energy at 600 K obtained from DFT calculations. This agreement explains the experimentally observed trend that the activation energy decreases as the number of CO ligands decreases. For the thermal decomposition of neutral $Ru(C_4H_6)(CO)_3$, the appearance of photoionized $Ru(C_4H_6)(CO)^+$ is a clear evidence of CO loss occurring at 740 K from $Ru(C_4H_6)(CO)_2$. The decomposition further proceeds above 800 K, forming $Ru(C_4H_6)$.

Author contributions

Data availability

The data supporting this article have been included as part of the ESI.†

Conflicts of interest

There are no conflicts to declare.

Acknowledgements

References

1 M. H. Hayes, C. L. Dezelah and J. F. Conley Jr., *ECS Trans.*, 2018, **85**, 743.

2 J. H. Han, S. W. Lee, G. J. Choi, S. Y. Lee, C. S. Hwang, C. Dussarrat and J. Gatineau, *Chem. Mater.*, 2009, **21**, 207–209.

3 H. J. Jung, J. H. Han, E. A. Jung, B. K. Park, J. H. Hwang, S. U. Son, C. G. Kim, T. M. Chung and K. S. An, *Chem. Mater.*, 2014, **26**, 7083–7090.

4 H. Kim, T. Koseki, T. Ohba, T. Ohta, Y. Kojima, H. Sato and Y. Shimogaki, *J. Electrochem. Soc.*, 2005, **152**, G594.

5 D. Josell, D. Wheeler, C. Witt and T. P. Moffat, *Electrochem. Solid-State Lett.*, 2003, **6**, C143.

6 P. Kumar, R. K. Gupta and D. S. Pandey, *Chem. Soc. Rev.*, 2014, **43**, 707.

7 D. E. Trent, B. Paris and H. H. Krause, *Inorg. Chem.*, 1964, **3**, 1057.

8 A. F. Bykov, N. B. Morozova, I. K. Igumenov and S. V. Sysoev, *J. Therm. Anal.*, 1996, **46**, 1551–1565.

9 R. Gaur, L. Mishra, M. A. Siddiqi and B. Atakan, *RSC Adv.*, 2014, **4**, 33785–33805.

10 T. Aoyama and K. Eguchi, *Jpn. J. Appl. Phys.*, 1999, **38**, L1134–L1136.

11 D. Z. Austin, M. A. Jenkins, D. Allman, S. Hose, D. Price, C. L. Dezelah and J. F. Conley Jr., *Chem. Mater.*, 2017, **29**, 1107–1115.

9250 | *Phys. Chem. Chem. Phys.*, 2025, **27**, 9244–9251

This journal is © the Owner Societies 2025

12 D. Z. Austin, M. A. Jenkins, D. Allman, S. Hose, D. Price, C. L. Dezelah and J. F. Conley Jr., *Chem. Mater.*, 2018, **30**, 8983–8984.

13 Z. Gao, D. Le, A. Khaniya, C. L. Dezelah, J. Woodruff, R. K. Kanjolia, W. E. Kaden, T. S. Rahman and P. Banerjee, *Chem. Mater.*, 2019, **31**, 1304–1317.

14 S. Cwik, K. N. Woods, M. J. Saly, T. J. Knisley and C. H. Winter, *J. Vac. Sci. Technol., A*, 2020, **38**, 012402.

15 M. Hayes, M. A. Jenkins, J. Woodruff, D. F. Moser, C. L. Dezelah and J. F. Conley Jr., *J. Vac. Sci. Technol., A*, 2021, **39**, 052402.

16 J. R. Schneider, C. de Paula, J. Lewis, J. Woodruff, J. A. Raiford and S. F. Bent, *Small*, 2022, **18**, 2105513.

17 K. Miyajima and F. Mafuné, *Chem. Phys. Lett.*, 2022, **786**, 139191.

18 Y. Kotsugi, S.-M. Han, Y.-H. Kim, T. Cheon, D. K. Nandi, R. Ramesh, N.-K. Yu, K. Son, T. Tsugawa, S. Ohtake, R. Harada, Y.-B. Park, B. Shong and S.-H. Kim, *Chem. Mater.*, 2021, **33**, 5639–5651.

19 E. Hückel, *Z. Phys.*, 1931, **70**, 204–286.

20 P. Dowd, *Acc. Chem. Res.*, 1971, **5**, 242–248.

21 L. M. Fillman and S. C. Tang, *Thermochim. Acta*, 1984, **75**, 71–84.

22 M. D. Jones, R. D. W. Kemmitt and A. W. G. Platt, *J. Chem. Soc., Dalton Trans.*, 1986, 1411–1418.

23 G. E. Herberich and T. P. Spaniol, *J. Chem. Soc., Dalton Trans.*, 1993, 2471–2476.

24 K. Miyajima and F. Mafuné, *J. Phys. Chem. A*, 2015, **119**, 8055–8061.

25 M. J. Frisch, G. W. Trucks, H. B. Schlegel, G. E. Scuseria, M. A. Robb, J. R. Cheeseman, G. Scalmani, V. Barone, G. A. Petersson, H. Nakatsuji, X. Li, M. Caricato, A. V. Marenich, J. Bloino, B. G. Janesko, R. Gomperts, B. Mennucci, H. P. Hratchian, J. V. Ortiz, A. F. Izmaylov, J. L. Sonnenberg, D. Williams-Young, F. Ding, F. Lipparini, F. Egidi, J. Goings, B. Peng, A. Petrone, T. Henderson, D. Ranasinghe, V. G. Zakrzewski, J. Gao, N. Rega, G. Zheng, W. Liang, M. Hada, M. Ehara, K. Toyota, R. Fukuda, J. Hasegawa, M. Ishida, T. Nakajima, Y. Honda, O. Kitao, H. Nakai, T. Vreven, K. Throssell, J. A. Montgomery Jr, J. E. Peralta, F. Ogliaro, M. J. Bearpark, J. J. Heyd, E. N. Brothers, K. N. Kudin, V. N. Staroverov, T. A. Keith, R. Kobayashi, J. Normand, K. Raghavachari, A. P. Rendell, J. C. Burant, S. S. Iyengar, J. Tomasi, M. Cossi, J. M. Millam, M. Klene, C. Adamo, R. Cammi, J. W. Ochterski, R. L. Martin, K. Morokuma, O. Farkas, J. B. Foresman and D. J. Fox, *Gaussian 16 Revision C.01*, Gaussian Inc., Wallingford CT, 2016.

26 E. Glendening, A. Reed, J. Carpenter and F. Weinhold, *NBO Version 3.1*.

27 A. E. Reed, R. B. Weinstock and F. Weinhold, *J. Chem. Phys.*, 1998, **83**, 735.

28 G. F. Emerson, K. Ehrlich, W. P. Giering and P. C. Lauterbur, *J. Am. Chem. Soc.*, 1966, **88**, 3172–3173.

29 W. Strohmeier and G. Schönauer, *Z. Naturforsch. B*, 1962, **17**, 848–854.

30 Q. Fan, H. Feng, W. Sun, Y. Xie, R. B. King and H. F. Schaefer III, *Organometallics*, 2012, **31**, 3610–3619.

31 R. A. Marcus, *J. Chem. Phys.*, 1965, **43**, 2658–2661.

32 R. A. Marcus, *J. Chem. Phys.*, 1970, **52**, 1018.

33 R. H. Schultz, K. C. Crellin and P. B. Armentrout, *J. Am. Chem. Soc.*, 1991, **113**, 8590–8601.

34 F. A. Khan, D. E. Clemmer, R. H. Schultz and P. B. Armentrout, *J. Phys. Chem.*, 1993, **97**, 7978–7987.

35 S. M. Lang, K. Miyajima, T. M. Bernhardt, F. Mafuné, R. N. Barnett and U. Landman, *Phys. Chem. Chem. Phys.*, 2018, **20**, 7781–7790.

36 T. Nagata, K. Miyajima and F. Mafuné, *J. Phys. Chem. A*, 2015, **119**, 10255–10263.

37 R. Wesendrup and H. Schwarz, *Organometallics*, 1997, **16**, 461–466.

38 A. Schneider, N. Popovska, I. Jipa, B. Atakan, M. A. Siddiqi, R. Siddiqui and U. Zenneck, *Chem. Vap. Deposition*, 2007, **13**, 389–395.

This journal is © the Owner Societies 2025

Phys. Chem. Chem. Phys., 2025, **27**, 9244–9251 | 9251